International Journal of Heat and Mass Transfer 52 (2009) 2849–2857

Contents lists available at ScienceDirect

International Journal of Heat and Mass Transfer

journal homepage: www.elsevier.com/locate/ijhmt

Solar pond modeling with density and viscosity dependent on temperature and salinity

M.C. Giestas [b,*], Heitor L. Pina [a], Jorge P. Milhazes [b], Célia Tavares [b]

[a] IDMEC Instituto Superior Técnico, Av.Rovisco Pais, 1049-001 Lisboa, Portugal
[b] INETI Est. do Paço do Lumiar 22, 1649-038 Lisboa, Portugal

ARTICLE INFO

Article history:
Received 18 June 2008
Available online 21 February 2009

Keywords:
Solar ponds
Convection
Double diffusion
Spectral methods
ODEs

ABSTRACT

The paper presents a 2D numerical model where the behavior of a salt gradient solar pond (SGSP) is described in terms of temperature, salt concentration and velocity with the fluid density and viscosity dependent on temperature and salt concentration. The discretization of the governing equations is based on the respective weak formulations. The rectangular geometry allows for spectral type Galerkin approximations for which the essential homogeneous boundary conditions can easily be imposed. Taking into account the variation of density and viscosity with temperature and salinity improved the agreement between the numerical and the experimental results.

© 2009 Elsevier Ltd. All rights reserved.

1. Introduction

A salt gradient solar pond (SGSP) is a basin containing a mixture of water and salt heated by solar radiation and used as an energy storage device. A temperature gradient (hotter at the bottom and cooler at the top) is established and a salt concentration gradient (denser at the bottom and lighter at the top) is therefore created and supposed to prevent convective motions that would otherwise promote the return of the stored energy to the outside ambient and thus destroying the pond's very purpose. A double diffusion process occurs where the temperature and salinity fields make opposite contributions to the fluid density.

There have been several attempts for the numerical solution of the governing equations. For example, Hull [1], Hawlader and Brinkworth [2] and Rubin et al. [3] have applied a finite difference method while [4] has used a finite element technique. The pond stability that constitutes one of the key factors governing a SGSP performance has been studied by several researchers who have resorted in most cases to the linear perturbation theory, see in particular [5–8] and [9]. The results obtained from these studies have provided important information regarding the onset of the instabilities as well as the existence of several possible stable or unstable states that may arise.

Weinberger [10] was the first to give a mathematical formulation of the behavior of a salinity gradient solar pond, analyzing among other things the absorption of the solar radiation by the brine solution, the losses to the atmosphere and to the ground and the double diffusion effect. The analytical solution of the partial differential equations for the transient temperature distribution was obtained by superposing the effects of the radiation absorption at the surface, in the body of water and at the bottom.

Meyer [11] developed a numerical model to predict the time dependent behavior of the interface between the convecting and the non-convecting regions of the solar pond. The model utilizes the empirical correlations that describes the heat and the salt fluxes across the interfaces of the pond regions.

Panahi et al. [12] employed a one-dimensional model to simulate the dynamic performance of the salinity gradient solar pond with a finite element technique.

Angeli and Leonardi [13] and [14] investigated the development of salt concentration profiles in a SGSP and studied the salt diffusion and stability of the density gradient. The prediction of the solar pond stability and performance was made by calculating the optimum salinity gradient thickness and its transient behavior taking into account the seasonal changes of both solar radiation and solar pond temperature (see also [15]).

Mansour et al. [16] solved numerically the problem of transient heat and mass transfer and long term stability of a SGSP through a 2D model and a finite volume method.

In theoretical stability studies, the vertical gradients of temperature and salt concentration are usually assumed constant as this facilitates the analysis, see [17–19,11,8,9].

However, in reality the viscosity may depend strongly on temperature and salt concentration, exponentially or even super-exponentially. In the case of solar ponds, where the temperature can range typically from 90 °C at the bottom and 20 °C at the top, the

* Corresponding author. Tel.: +351 21 7127181; fax: +351 21 7127195.
E-mail addresses: margarida.giestas@ineti.pt (M.C. Giestas), hpina@dem.ist.utl.pt (H.L. Pina).

0017-9310/$ - see front matter © 2009 Elsevier Ltd. All rights reserved.
doi:10.1016/j.ijheatmasstransfer.2009.01.003

Nomenclature

a	scalar field, Eq. (1)
a, b, c, d	fitting parameters, Eq. (16)
C_p	specific heat [J/kg°C]
$\mathbf{g}$	gravity acceleration [m/s^2]
h	convection coefficient, Eq. (3) [w/mk]
L_1, L_2	domain length and height
$\mathbf{n}$	unit vector
p	pressure [N^2/m]
q	flux, Eq. (2)
S	salt concentration [kg/m^3]
T	temperature [K]
$\mathbf{T}$	viscous stress tensor, Eq. (5)
t	time [s]
u	generic scalar field, Eq. (1)
$\mathbf{v}$	velocity field [m/s]
$\mathbf{x} = (x_1, x_2)$	Cartesian co-ordinates

Greek symbols

α_S	salt diffusivity [m^3/kg]
α_T	thermal diffusivity [K^{-1}]
∂	partial derivative
μ	dynamic viscosity [m^2/s]
γ	convection coefficient, Eq. (3) [W/m^{2}k]
Ω	domain
Γ	boundary of Ω
ν	kinematic viscosity[m^2/s]
ψ	stream function
θ	dimensionless temperature
ω	dimensionless concentration
ρ	fluid density[kgm^3]
σ	coefficient, Eq. (1)
∇	gradient
$\nabla\cdot$	divergence

Subscripts

1, 2, 3, 4	ith face of the domain Ω
amb	ambient
0	initial
f	final
S	salt
T	temperature

Superscripts

$\dot{y}$	time derivative
$\mathbf{v}^{\mathrm{T}}$	transpose

viscosity can vary by one order of magnitude and in many industrial and geophysical applications even much more. In stability studies this implies the base state to depart from constant temperature and salinity gradients. Concerning the case of linear stability, perturbations are assumed to be infinitesimal and then they act with constant viscosity over a base state calculated with a variable viscosity. However, if a full nonlinear analysis is envisaged, the perturbations are no longer infinitesimal and the viscosity variation has to be dully accounted for as was shown both theoretically and experimentally by [20] in the context of a Rayleigh–Bénard problem with glycerol. The observations of [21] show that in a real solar pond the salt gradient is far from constant. In [22] the effect of a constant temperature gradient but a variable vertical salt gradient on the stability of a fluid layer was considered. An experimental programme to assess the various configurations at the onset of convection in the presence of temperature dependent viscosity was carried out by [23].

A linear stability study with variable fluid properties and a nonlinear basic salt concentration was presented in [24] for a horizontally infinite fluid layer subject to small perturbations. In [25,26] the effect of a exponentially temperature dependent viscosity in natural convection for high or infinite Prandtl number is assessed and comparisons with the case of constant viscosity are presented. The control of a SGSP to ensure successful year round operation was studied in [27] employing a one-dimensional model and is typical of the practical difficulties facing a realistic modeling of such devices.

The present paper considers a rectangular cavity filled with either glycerin or a mixture of water and salt (sodium chloride, NaCl) heated at the bottom. The fluids are treated as newtonian incompressible, heat conducting according to Fourier's law and the salt diffusion obeys Fick's law and are subject to a uniform gravitational field. The density is given by the usual linear Boussinesq type approximation and the viscosity by a nonlinear function of the temperature and salinity.

The discretization of the governing equations is based on the respective weak formulations. The rectangular geometry allows for spectral type approximations for which the essential homogeneous boundary conditions can easily be imposed. This choice of method is justified not as much from the outstanding accuracy spectral methods can achieve but rather to obtain a moderate accuracy employing instead a modest number of spatial modes which nevertheless may prove to be adequate for SGSP modeling.

The numerical model developed simulates the three zones that characterize a SGSP attempting to capture the boundary zones behavior by using a non-uniform nodal distribution (Gauss–Legendre–Lobatto nodes).

1.1. Notation

A cartesian coordinate system is employed throughout with position given by $\mathbf{x} = (x_1, x_2)$ and time is denoted by t.

The domain for the examples in Section 4 is a rectangle $\Omega = [0, L_1] \times [0, L_2]$ as depicted in Fig. 1. Its boundary is $\partial\Omega = \bigcup_{i=1}^{4} \Gamma_i$, where the Γ_i are the faces (Γ_1 is on the plane $x_1 = 0$, Γ_2 on the plane $x_1 = L_1$, Γ_3 on the plane $x_2 = 0$ and Γ_4 on the plane $x_2 = L_2$).

2. The governing equations

2.1. The diffusion equations

The two diffusion equations for the temperature T and for the salt concentration S are of the following type

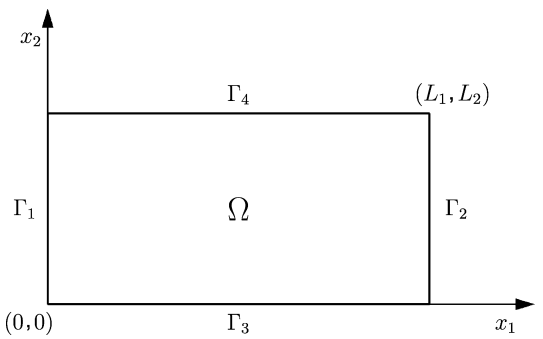

Fig. 1. Geometry and notation.

$$\sigma(\partial_t u + \mathbf{v}\cdot\nabla u) = \nabla\cdot\mathbf{q}, \quad \text{in } \Omega \tag{1}$$

Here $u = u(\mathbf{x},t)$ represents the scalar field, $\mathbf{v} = \mathbf{v}(\mathbf{x},t)$ is the fluid velocity, $\sigma > 0$ is a scalar and $a(\mathbf{x}) > 0$ is a scalar field. The flux vector is of Fourier or Fick type

$$\mathbf{q} = -\nabla(au) \tag{2}$$

The boundary (BC's) and initial (IC) conditions considered are

$$\begin{aligned} &u = 0, \quad \text{on } \partial\Omega_0 \ \text{(essential BC's)}\\ &a\partial_n u + hu = \gamma, \quad \text{on } \partial\Omega_1 \ \text{(natural BC's)}\\ &u(\mathbf{x},0) = u_0(\mathbf{x}), \quad \text{in } \Omega \end{aligned} \tag{3}$$

We note that the essential BC's are homogeneous; non-homogeneous BC's will be addressed later.

2.2. The balance of momentum

The fluid is assumed to be newtonian and incompressible. However, the density ρ in the buoyancy term (see below) and the viscosity ν are taken to depend on the several diffusion components present (temperature and salinity).

The balance of linear momentum delivers the Navier–Stokes equations

$$\rho(\partial_t\mathbf{v} + (\nabla\mathbf{v})\mathbf{v}) = -\nabla p + \nabla\cdot(2\mu\mathbf{D}) + \rho\mathbf{b}, \quad \text{in } \Omega \tag{4}$$

where

$$\mathbf{D} = \frac{1}{2}(\nabla\mathbf{v} + (\nabla\mathbf{v})^{\mathrm{T}}), \quad \mathbf{T} = 2\mu\mathbf{D} \tag{5}$$

denote the strain rate and stress tensors.

The incompressibility condition is expressed by

$$\nabla\cdot\mathbf{v} = 0, \quad \text{in } \Omega \tag{6}$$

The boundary (BC's) and initial (IC) conditions considered are

$$\begin{aligned} &\mathbf{v} = \mathbf{0}, \quad \text{on } \partial\Omega_0 \quad \text{(essential BC's)}\\ &\mathbf{v}\cdot\mathbf{n} = 0 \quad \text{and} \quad \mathbf{t}\cdot\mathbf{n} = 0 \quad \text{on } \partial\Omega_1 \quad \text{(natural BC's)}\\ &\mathbf{v}(\mathbf{x},0) = \mathbf{v}_0(\mathbf{x}), \quad \text{in } \Omega \end{aligned} \tag{7}$$

We note that all the BC's are homogeneous.

2.3. The Boussinesq approximation and variable viscosity

The Boussinesq approximation the density consists in taking ρ in the LHS of (4) as constant and equal to some reference value ρ_0 but allowing it to depend on the diffusive components in the term $\rho\mathbf{b}$ in the RHS of (4).

In the presence of R diffusive components, the Boussinesq approximation consists in making a linear approximation on ρ by declaring that

$$\frac{\rho}{\rho_0} = 1 - \sum_{r=1}^{R}\alpha_r(u_r - u_{r0}) \tag{8}$$

where the α_r is a constant coefficient relative to the component r and ρ_0, u_0 are reference values. Specifically, for the case of temperature T and salt concentration S, expression (8) amounts to

$$\frac{\rho}{\rho_0} = 1 - \alpha_T(T - T_0) - \alpha_S(S - S_0) \tag{9}$$

The term $\rho\mathbf{b}$ in the right hand side of (4) is in our case the force due to gravity. From the Boussinesq type approximation (8) it follows that

$$\frac{\rho}{\rho_0}\mathbf{b} = \left(1 - \sum_{r=1}^{R}\alpha_r(u_r - u_{r0})\right)\mathbf{g} \tag{10}$$

Introducing this relation in (4) we get

$$\partial_t\mathbf{v} + (\nabla\mathbf{v})\mathbf{v} = -\nabla p' + \nabla\cdot(2\nu\mathbf{D}) + \mathbf{b}' \tag{11}$$

with

$$\begin{aligned} p' &= \frac{p}{\rho_0} + \left(1 - \sum_{r=1}^{R}\alpha_r u_{r0}\right)(\mathbf{g}\cdot\mathbf{x})\\ \mathbf{b}' &= -\sum_{r=1}^{R}\alpha_r u_r\mathbf{g} \end{aligned} \tag{12}$$

We assume that the kinematic viscosity is given by

$$\nu = \nu_0 f(u_0,\ldots,u_R) \tag{13}$$

3. Discretization

3.1. The weak formulation

The weak form of (1) and (4) are obtained by multiplying both of its members by test functions, integrating in Ω and applying integration by parts to decrease the order of the derivatives of u involved (see, for instance [28] for details).

3.2. Basis functions

The domains Ω we are interested in are cartesian products of intervals, so we construct basis functions in a systematic way as tensor products of univariate functions. These basis possess the regularity required by the weak forms (in fact, they belong to $C^\infty(\Omega)$) and are constructed to satisfy the essential homogeneous boundary conditions thereby generating admissible trial spaces.

For the examples treated we employed for trial and test functions tensor products of Lagrange polynomials with Gauss–Legendre–Lobatto nodes (see [29–31]) or modifications thereof whenever compliance with homogeneous essential boundary conditions was required.

To identically satisfy the incompressibility condition (6), the velocity basis functions were expressed in terms of a stream functions basis functions ψ, by putting $\mathbf{v} = (\partial_{x_2}\psi(x_1,x_2), -\partial_{x_1}\psi(x_1,x_2))$ thereby effecting a considerable simplification by eliminating the pressure term from the problem formulation.

3.3. The ODE's system

The ODE's systems resulting from the space discretization of the diffusion and momentum equations yield after assemblage a global system of ODE's that we write as

$$\dot{\mathbf{y}}(t) = \mathbf{f}(\mathbf{y}(t)), \quad \mathbf{y}(0) = \mathbf{y}_0 \tag{14}$$

where $\mathbf{y}$ denotes the time dependent coefficients and $\mathbf{y}_0$ is the coefficient vector obtained by interpolation of the initial conditions.

This ODE system is moderately stiff and the BDF (Backward Differentiation Formula) method together with a variable step-variable order algorithm designed to satisfy user specified error tolerances as implemented in the subroutine VODE (see [32]) was employed for its solution.

4. Results

The richness of the convection patterns found in Rayleigh–Bénard problems is enormous (see [33, Ch. 6] for a thorough discussion and references). Here we are interested in obtaining the equilibrium states defined as the zeros of the right hand side $\mathbf{f}(\mathbf{y}(t))$ of (14) namely to assess their nature, wether they are sta-

tionary or oscillatory, which convection roll patterns they allow, etc.

We reach these states by integrating the ODE system (14) for $t \in (0, t_f]$ for t_f sufficiently large to reach a steady state and paying attention to the transient regimes insofar as they may condition the selection of final states actually reached.

These steady states depend crucially on the spectrum of the jacobian of $\mathbf{f}(\mathbf{y}(t))$ and its impact on the time integration method eventually leading for certain combination of modes to divergence (if an eigenvalue with positive real part is present) or to convergence towards spurious states, i.e., states not allowed by the original partial differential equations system and are a consequence instead of the specifics of the space discretization employed. This perplexing phenomena being attributable to the presence of convective terms have been referred to in the literature as "approximation instabilities" to distinguish them from the instabilities associated with time-discretization schemes (see [31, Ch. 4] for a study applied to the advection–diffusion equation and references therein for possible remedies to this problem).

Experiments employing the PIV (Particle Image Velocimetry) technique to measure instantaneous velocity fields and to detect spatial flow structures [34] are used to validate the numerical results.

We present and discuss results for the two cases

- Glycerin (99%) and water (1%) (to be denoted by G);
- Salted water (to be denoted by S).

and the following notation is used to refer to numerical and experimental results

- Numerical results for Glycerin NG and experimental data for Glycerin DG;
- Numerical results for salted water NS and experimental data for salted water DS.

The boundary conditions are

- for temperature: Γ_1 and Γ_2 are insulated (zero heat flux), and Γ_4 has thermal losses due to radiation and convection and also due to evaporation in the S case; Dirichlet type on Γ_3 where a constant temperature $T_3 = 50\ ^\circ\mathrm{C}$ is imposed;
- for salinity: zero salt flux on all boundaries;
- for velocity: zero velocity on Γ_1, Γ_2 and Γ_3 and a stress-free condition on Γ_4.

Table 1
Data used in the examples.

	Units	Case G	Case S
L_1, L_2	m	0.1	0.1
ρ	kg/m^3	1259	1021
C_p	J/m^3 °C	2620	3740
ν_0	m^2/s	1.4×10^{-4}	0.58×10^{-6}
α_S	m^3/kg	–	-0.64×10^{-3}
α_T	K^{-1}	5.4×10^{-4}	4.5×10^{-4}
σ_S		–	1
σ_T	J/m^3 °C	3.3×10^6	3.8×10^6
T_3	K	323	323
T_{amb}	K	299	292
$\mathbf{v}_0$	m/s	0	0
T_0	K	T_{amb}	T_{amb}
S_0	kg/m^3	–	$51 - 44.9x_2/L_2$
T: $h_1 = h_2$	W/m^{2}K	4.13	4.12
T: h_4	W/m^{2}K	7.84	14.89
T: $\gamma_1 = \gamma_2$	W/m^{2}K	1201	1205
T: γ_4	W/m^{2}K	2349	4533
S: $h_1 = h_2 = h_3 = h_4$	W/m^{2}K	0	0
S: $\gamma_1 = \gamma_2 = \gamma_3 = \gamma_4$	W/m^2 K	0	0
t_f	s	10^4	6.3×10^4

The initial conditions are:

- for temperature: $T(0, \mathbf{x}) = T_{amb}$;
- for salinity: $S(0, \mathbf{x}) = 51 - 44.9x_2/L_2$;
- for velocity: $\mathbf{v}(0, \mathbf{x}) = \mathbf{0}$.

A nonlinear least square fit to the International Critical Tables for a temperature range of 5–100 °C gives the following relation for the viscosity for the G case

$$v(T) = \frac{1}{\rho_0}\left(a + b\exp\left(-\frac{T}{c}\right)\right) \tag{15}$$

with $a = 0.095010192$, $b = 11.992008$ and $c = 9.1165079$. The viscosity for the S case is given by

$$10^6 v(T, S) = a\exp(-bT) + c\exp(-dS) \tag{16}$$

with $a = 1.63919$, $b = 0.03215$, $c = 0.169423$ and $d = -0.0489519$. Other data employed in the examples are collected in Table 1.

For the case NG a spatial discretization of $(8 \times 16, 8 \times 16)$ was employed (8 modes in the x_1 direction and 16 in the x_2 direction for both the velocity and temperature). However, taking in account the boundary conditions imposed, these correspond to $(6 \times 14, 8 \times 15)$ basis functions, leading to a total of 84° of freedom for velocity and 120° of freedom for temperature. For the case NS

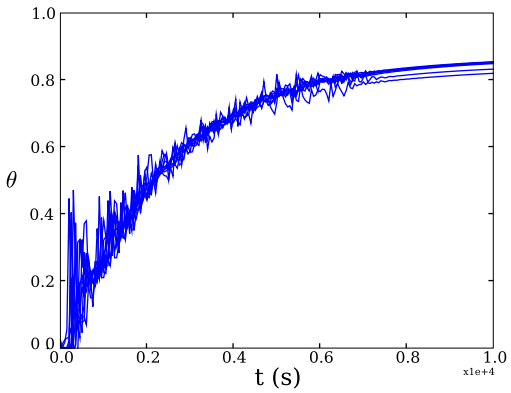

2.1: NG: Temperature at different depths

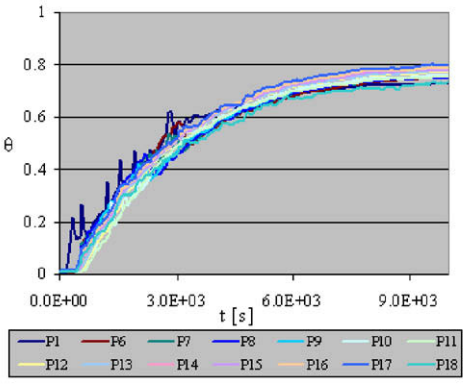

2.2: DG: Temperature at different depths

Fig. 2. Temperature time evolution.

Table 2
G: Steady state heat fluxes.

Heat flux (W/m^2)	G – v constant	G – v variable
$q_1 = q_2$	2.47	2.47
q_3	−6.30	−7.40
q_4	1.62	1.40

Table 3
G: Maximum and average velocities.

Vel. (m/s)	NG	DG
Max.	1.0×10^{-2}	0.4×10^{-2}
Avg.	0.5×10^{-3}	0.8×10^{-3}

the same domain discretization was used $(8 \times 16, 8 \times 16, 8 \times 16)$ the last group 8×16 pertaining to the salinity, resulting in 84 degrees of freedom for velocity, 120 for temperature and 128 for salinity making a total of 332 degrees of freedom.

In order to assess the dependency of the results on the discretization several runs were made employing a larger number of degrees of freedom. The results did not change appreciably but a much larger computer time was required. The discretizations above seem to be sufficiently accurate given all the modeling assumptions made.

For the sake of presentation of results, the temperature is adimensionalised as

$$\theta = T \rightarrow \frac{T - T_{amb}}{T_3 - T_{amb}} \tag{17}$$

and salinity as

$$\omega = S \rightarrow \frac{S - S_4}{S_3 - S_4} \tag{18}$$

4.1. Cases NG and DG

For these cases experiments showed that the stationary state was reached at $t_f \approx 10^4$ s which has been adopted also for the numerical simulations.

4.1.1. Temperature

Figs. 2.1 and 2.2 depict the temperature evolution at different depths. In Fig. 2.1 the temperature was obtained in steps of i C. In the experimental setup the temperature was measured by 18 probes (P1–P18) and is shown in Fig. 2.2. The line denoted by P1 corresponds to a temperature measured near the bottom and the line denoted by P18 to the temperature measured near the top.

The temperature time evolution is similar for the NG and DG cases, the steady state reached at about 10^4 S in both situations. At the central line $x_1 = L_1/2$ we obtained $T_4 - T_3 = 1.3\ ^\circ$C for NG

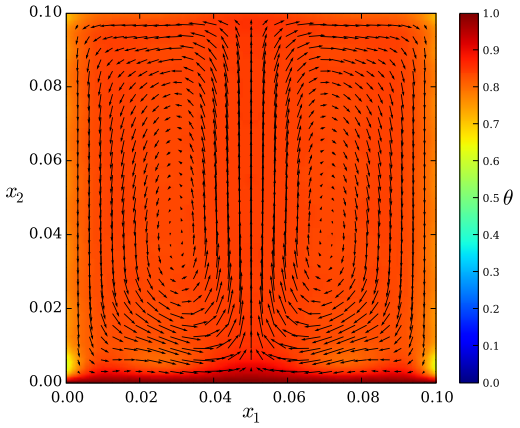

3.1: NG: Velocity and temperature fields

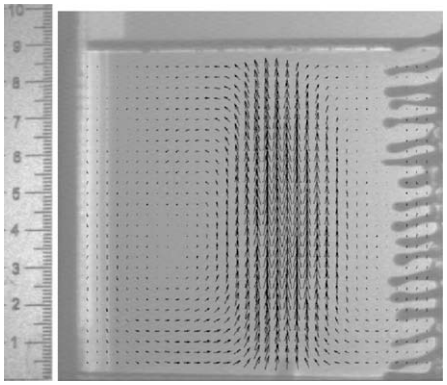

3.2: DG: Velocity field

Fig. 3. G: Velocity field at $t_f = 10^4$s.

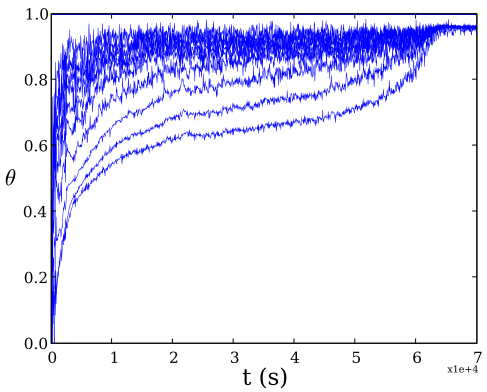

4.1: NS: Temperature at different depths

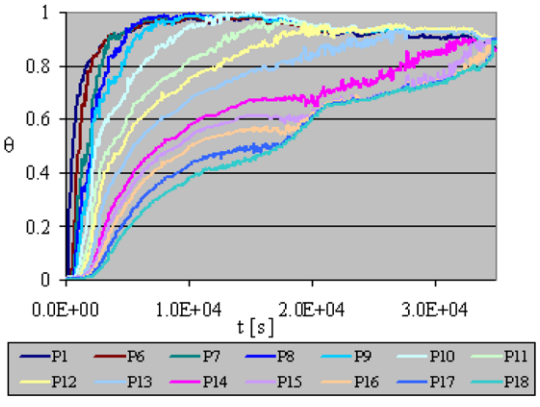

4.2: DG: Temperature at different depths

Fig. 4. S: Temperature time evolution.

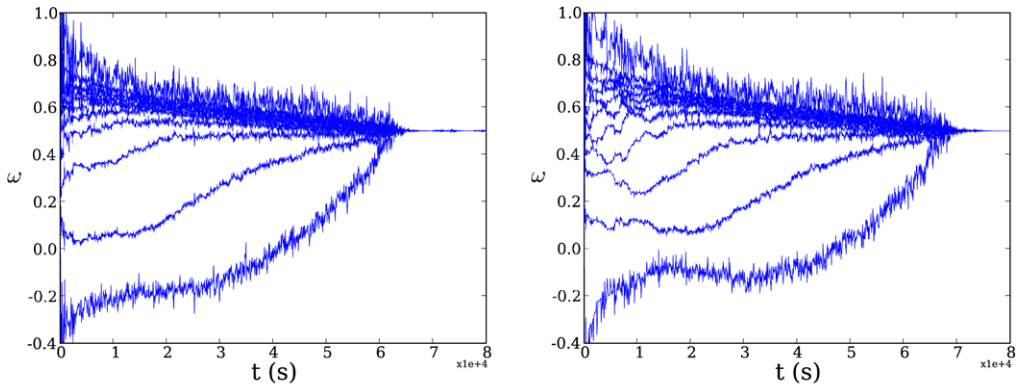

5.1: NS: Variable viscosity 5.2: NS: Constant viscosity

Fig. 5. NS: Salinity time evolution.

Table 4
S: Steady state heat fluxes.

Heat flux (W/m^2)	S – ν constant	S – ν variable
$q_1 = q_2$	0.13	0.25
q_3	−5.51	−4.42
q_4	0.94	1.07

and $T_4 - T_3 = 1.2\,^{\circ}$C for DG thus confirming an almost homogeneous steady state. The steady heat losses presented in Table 2 are almost the same wether the viscosity is constant or variable.

4.1.2. Velocity

Figs. 3.1 and 3.2 depict the convection cells configuration superposed with the temperature field for NG and superposed to a shadowgraph image for DG, both at the final stationary state. Again no

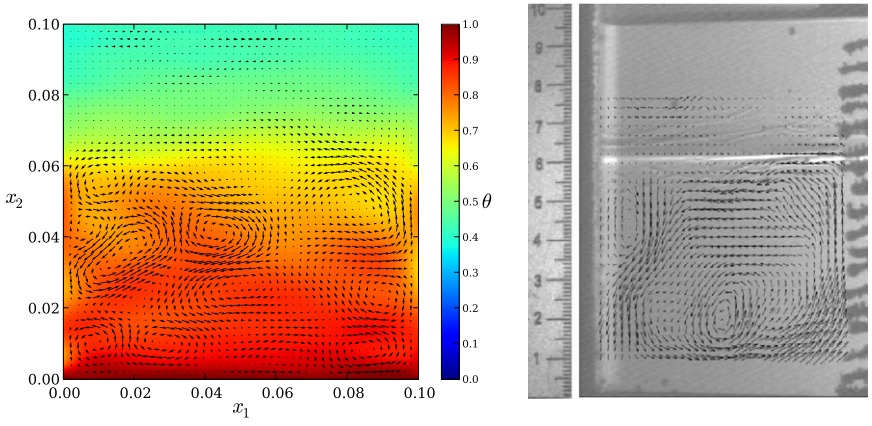

6.1: NS: Velocity and temperature at 3.8 $\times 10^3$ s 6.2: DS: Velocity field

Fig. 6. Convection cells at 6 cm height.

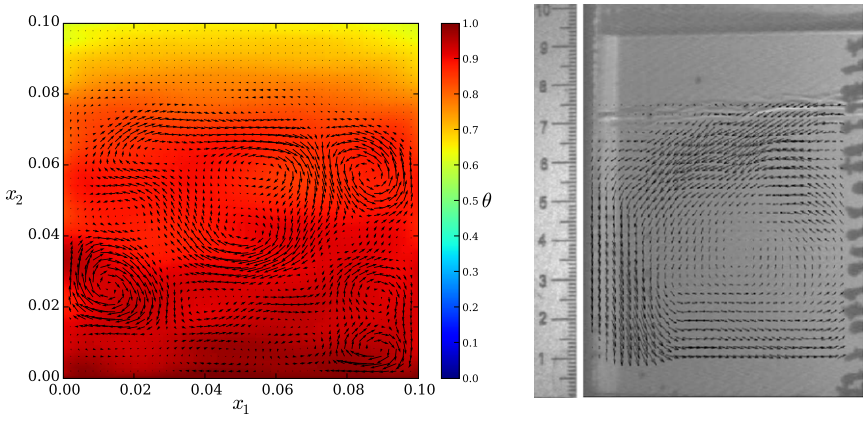

7.1: NS: Velocity and temperature at 3.12 $\times 10^4$ s 7.2: DG: Velocity field

Fig. 7. Convection cells at 7.5 cm height.

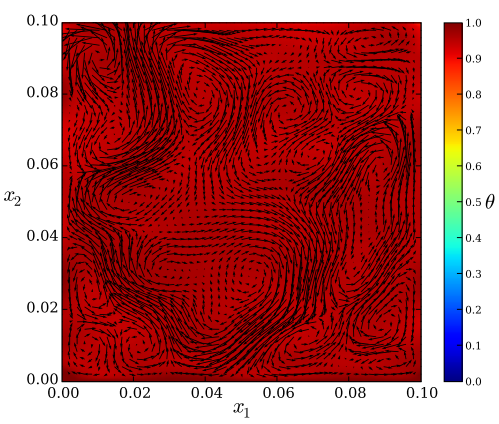

8.1: NS: Velocity and temperature fields

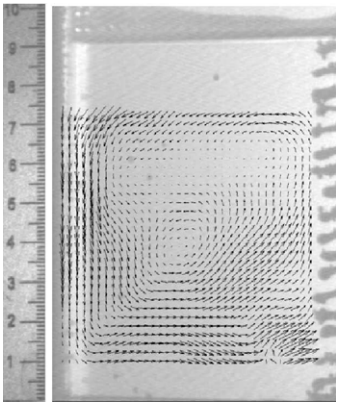

8.2: DG: Velocity field

Fig. 8. Convection cells at stationary state.

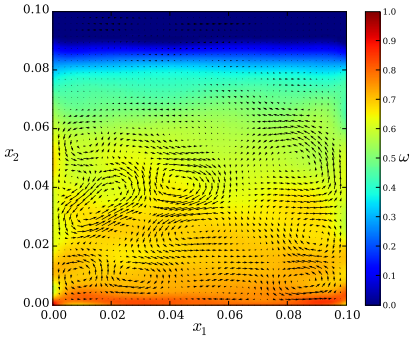

9.1: NS: Convection cells at 6 cm height, 3.8×10^3 s

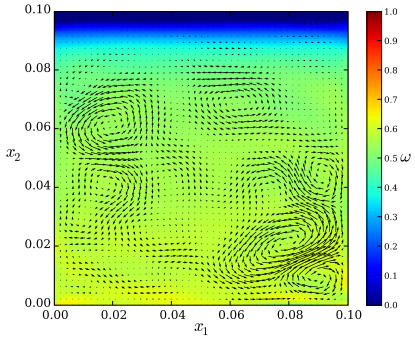

9.2: NS: Convection cells at 7.5 cm, 3.12×10^4 s

Fig. 9. Velocity and salinity fields.

appreciable difference between NG and DG is detected. Fig. 3.1 also shows the temperature profile $x_1 = L_1/2$ at the stationary sate.

Table 3 shows the maximum and average velocities for NG and DG at the stationary state. There is no appreciable difference between the velocities obtained numerically and measured experimentally.

Both temperature and velocity values for the G case show a reasonable agreement between the numerical and the experimental results which seem to validate the numerical model developed thus instilling confidence for the more demanding S case.

4.2. Cases NS and DS

The numerical results for the salted water case are presented for the time $t_f = 6.3 \times 10^4$ s substantially greater than the time $t_f = 4 \times 10^4$ s required in the experiments to reach the steady state. This discrepancy will be addressed below.

4.2.1. Temperature and salinity

The temperature evolution at different depths is presented in Figs. 4.1 and 4.2. These evolutions look similar and at $x_1 = L_1/2$ we have $T_4 - T_3 \approx 1\,^\circ$C at the stationary state for both the NS and DS cases.

The salinity evolution for the NS case, Fig. 5.1, agrees with Fig. 4.1, the salinity homogenization occurring at about the same time as the temperature's. We also present the salinity time evolution for the constant viscosity case in Fig. 5.2. Both Figs. 5.1 and 5.2 point to a qualitatively similar behavior. However, Fig. 5.2 shows that the homogenization is achieved at a later time of approximately 7×10^4 s.

Table 4 shows the differences in the steady heat fluxes when considering ν constant or variable, this later case yielding slightly larger heat losses at the surface.

4.2.2. Convection patterns

Figs. 6.1–8.2 show the growth of the bottom convective zone which exhibits a steplike character.

Numerical simulations and experimental results are shown at the instants the convective zone reaches three depths: 6 cm, 7.5 cm and 10 cm, this last one corresponding to the final steady state.

Figs. 6.1, 7.1 and 8.1 show the velocity field superposed to the temperature field.

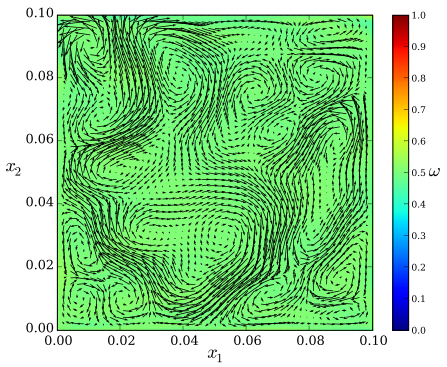

Fig. 10. Velocity and salinity fields at 6.3×10^4 s.

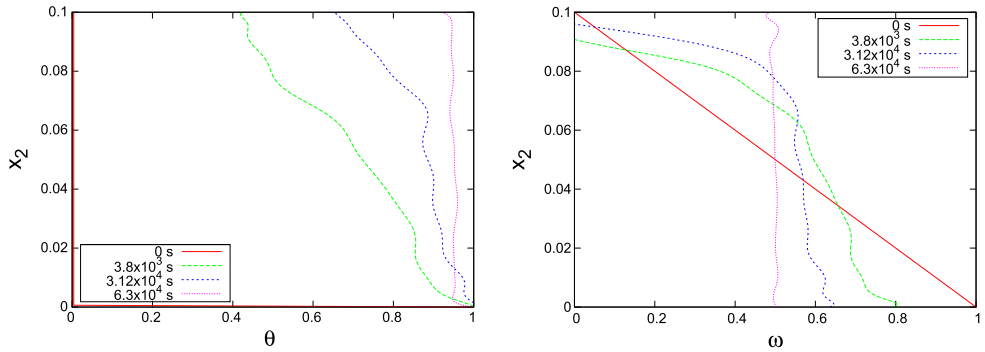

11.1: θ profile 11.2: ω profile

Fig. 11. θ and ω profiles at $t = \{0, 3.8 \times 10^3, 3.12 \times 10^4, 6.3 \times 10^4\}$ s.

Table 5
S: Maximum and average velocities.

Vel. (m/s)	NS	DS
Max.	0.7×10^{-2}	0.8×10^{-2}
Avg.	0.3×10^{-2}	0.3×10^{-2}

Experimental velocity fields obtained from PIV are presented superposed to the respective shadowgraph images. A ruler gives indication of the bottom convective zone evolution (see Figs. 6.2, 7.2 and 8.2).

Figs. 6.1–8.2 show the salinity gradient being destroyed in the process of reaching a homogeneous final state. This process can also be observed in Figs. 9.1–10 where the salinity evolution is depicted.

The salinity gradient becomes weaker at about 3800 s and the bottom convective zone begins to grow in a steplike fashion in accordance with the observations of [35]. A second step to 7.5 cm at about 31,200 s can be seen in Fig. 7.1. This growth can also be seen in the shadowgraph images Figs. 6.2, 7.2 and 8.2: two layers, the bottom one corresponding to a convection zone and the upper corresponding to a quiescent zone not yet reached by the convective movements. Convection cells grow to reach 10 cm at about 63,000 s corresponding to the steady state, see Figs. 9.1–10.

Figs. 11.1 and 11.2 show the temperature and salinity as a function of x_2 for $t = 0$ s, $t = 3800$ s and $t = 31{,}200$ s, these last two corresponding to the same instants as shown in Figs. 6.1 and 7.1, respectively. The homogeneous state is also represented for $t_f = 63{,}000$ s. The temperature and salinity profiles develop in accordance with similar results in [36–38,27,39] and [13].

Table 5 shows the maximum and average velocities for the NS and DS cases at the stationary state revealing similar values for these quantities.

5. Discussion and conclusions

For the NS and DS cases the temperature and salinity evolution are similar albeit the numerical model requires a longer time to reach the steady state than that measured in the experiments. This differences from $t_f \approx 4 \times 10^4$ s for the experiments and $t_f \approx 6.3 \times 10^4$ *rms* for the numerical simulation can be attributed to the following circumstances:

- three-dimensional effects present in the experiments but absent in the two-dimensional model imparting greater mobility to the fluid;
- the temperature at Γ_3 is constant in the model but the experimental setup is unable to precisely control this variable allowing for spatial and temporal temperature variation at Γ_3 to be about 1—2 °C;
- the numerical model for the S case considers thermal evaporation losses to the atmosphere at Γ_4 but disregards any associated mass transfer; however the shadowgraph images show that this mass transfer amounts to a reduction of about 1 cm in a 10 cm deep cavity which is not negligible. This hypothesis seems to be corroborated in the G case where no surface evaporation is present and the time of homogenization is similar for the NG and DG cases.

The introduction of variable viscosity in the model leads to the following effects on the heat fluxes. For the G case the fluxes are similar for variable or constant viscosity but for S case the heat flux at Γ_4 is slightly higher for variable viscosity than for constant viscosity. This stresses the importance of employing a realistic viscosity variation in assessing thermal losses at the surface of a SGSP.

The results for the NG and DG are similar and in this sense the experiments validate the numerical model. For the S case the evolution of the bottom convective zone and the onset of convection also agree for both numerical and experimental results. In the S case there is an influence of variable viscosity in the behavior of the fluid that justifies the computational complexity added to the numerical model.

We conclude that the numerical model developed employing a modest number of degrees of freedom is reasonably validated by the experimental data and thus can be used as a analysis tool for the design of SGPS.

Acknowledgments

The work reported was partially supported by FCT Project POCI/EME/58807/2004.

References

[1] J.R. Hull, Computer simulation of solar pond thermal behaviour, Solar Energy 25 (33) (1980).
[2] M.N.A. Hawlader, B.J. Brinkworth, An analysis of the non convecting solar pond, Solar Energy 27 (1981) 195–204.
[3] H. Rubin, B.A. Benedict, S. Bachu, Modeling the performance of a solar pond as a source of thermal energy, Solar Energy 32 (1984) 771–778.
[4] T.S. Jayadev, J. Henderson, Salt concentration gradient solar ponds, in: Modeling and Optimization, Colorado, 1979.
[5] G. Veronis, Effect of a stabilizing gradient of solute on thermal convection, J. Fluid Mech. 34 (1968) 315–336.
[6] L.N. Da Costa, E. Knobloch, N.O. Weiss, Oscillations in double-diffusive convection, J. Fluid Mech. 109 (257) (1981) 25–43.
[7] R.S. Schechter, M.G. Velarde, J.K. Platten, The two-component Bénard problem, Wiley, 1981.

[8] M. Giestas, A. Joyce, H. Pina, The influence of radiation absorption on solar ponds stability, Int. J. Heat Mass Transfer 39 (18) (1996) 3873–3885.
[9] M. Giestas, A. Joyce, H. Pina, The influence of non-constant diffusivities on solar ponds stability, Int. J. Heat Mass Transfer 40 (18) (1997) 4379–4391.
[10] H. Weinberger, The physics of the solar pond, Solar Energy 8 (2) (1964).
[11] K.A. Meyer, D.P. Grimmer, G.F. Jones, An experimental and theoretical study of salt-gradient pond interface behaviour, Progress in Solar Energy, 1982.
[12] Z. Panahi, J.C. Batty, J.P. Riley, Numerical simulation of the performance of a salt gradient solar pond, Trans. ASME J. Solar Energy Eng. 105 (1983) 361–374.
[13] C. Angeli, E. Leonardi, A one-dimensional numerical study of the salt diffusion in a salinity-gradient solar pond, Int. J. Heat Mass Transfer (47) (2004) 1–10.
[14] C. Angeli, E. Lombardi, The effect of thermodiffusion on the stability of a salinity gradient solar pond, Int. J. Heat Mass Transfer 48 (21–22) (2005).
[15] M. Karakilcik, K. Krymaç, I. Dincer, Experimental and theoretical temperature distributions in a solar pond, Int. J. Heat Mass Transfer 49 (5–6) (2005).
[16] Ridha Ben Mansour, Cong Tam Nguyen, Nicolas Galanis, Transient heat and mass transfer and long-term stability of a salt-gradient solar pond, Mech. Res. Commun. 33 (2006) 233–249.
[17] J.M.K. Dake, D.R.F. Harleman, Thermal stratification in lakes: analytical and laboratory studies, Water Resources Res. 5 (1969).
[18] A. Akbarzadeh, G. Ahmadi, Computer simulation of the performance of a solar pond in the southern part of Iran, Solar Energy 24 (1980).
[19] Y.S. Cha, W.T. Sha, W.W. Schertz, Modeling of the surface convective layer of salt gradient solar ponds, J. Solar Energy Eng. 104 (1982) 293–298.
[20] K.C. Stengel, D.S. Oliver, J.R. Booker, Onset of convection in a variable viscosity fluid, J. Fluid Mech. 120 (1982).
[21] F. Zangrando, Observation and Analysis of a Full-Scale Experimental Salt Gradient Solar Pond. PhD thesis, Department of Physics, University of New Mexico, 1979.
[22] I.C. Walton, Double-diffusive convection with large variable gradients, J. Fluid Mech. 125 (1982) 123–135.
[23] D.B. White, The planforms and onset of convection with a temperature-dependent viscosity, J. Fluid Mech. (191) (1988) 247–286.
[24] J. Tanny, V.A. Gotlib, Linear stability of a double diffusive layer with variable fluid properties, Int. J. Heat Mass Transfer 28 (9) (1995) 1683–1691.
[25] Y.Y. Jin, C.F. Chen, Natural convection of high Prandtl number fluids with variable viscosity in a vertical slot, Int. J. Heat Mass Transfer 39 (13) (1996) 2663–2670.
[26] A. Mambole, G. Labrosse, E. Tric, L. Fleitout, Linear stability of a double diffusive layer of an infinite Prandtl number fluid with temperature dependent viscosity, Stud. Geophys. Geod. 48 (2004) 519–537.
[27] M. Ouni, A. Guizani, H. Lu, A. Belghith, Simulation of the control of a salt gradient solar pond in the south of Tunisia, Solar Energy 75 (2003) 95–101.
[28] H. Pina, M. Giestas, A. Joyce, Modelação tridimensional de lagos solares, in: Congreso de Métodos Numéricos en Ingenieria, Granada, Espanha, 2005.
[29] J.P. Boyd, Chebyshev & Fourier Spectral Methods, Springer-Verlag, 1989.
[30] C. Canuto, M.Y. Hussaini, A. Quarteroni, T.A. Zang, Spectral Methods in Fluid Mechanics, Springer-Verlag, 1988.
[31] R. Peyret, Spectral Methods for Incompressible Viscous Flow, Springer-Verlag, 2002.
[32] G.D. Byrne, P.N. Brown, A.C. Hindmarsh, Vode, a variable-coefficient ode solver, SIAM J. Sci. Stat. Comput. 10 (1989) 1038–1051.
[33] A.V. Getling, Rayleigh–Bénard Convection: Structures and Dynamics, World Scientific, 1998.
[34] C. Tavares, E. Fernandes, D. Alves, J. Coelho, A. Joyce, Estudo de camadas duplamente difusivas: aplicação a lagos solares, CIES XIII Congresso Ibérico e VIII Congresso Ibero-Americano de Energia Solar, 2006.
[35] J.S. Turner, Multicomponent convection, Ann. Rev. Fluid Mech. 17 (1985) 11–14.
[36] M.R. Jaefarzadeh, A. Akbarzadeh, Towards the design of low maintenance salinity gradient solar ponds, Solar Energy 73 (5) (2002) 375–384.
[37] T. Radko, A mechanism for layer formation in a double diffusive fluid, J. Fluid Mech. (497) (2003) 365–380.
[38] D. Lohse, S. Grossman, On geometry effects in Rayleigh–Bénard convection, J. Fluid Mech. (486) (2003) 105–114.
[39] M.R.I. Ramadan, A.M. Khallaf, S.A. Enein, A.A.E. Sabaii, Parametric study of a shallow solar pond under the batch mode of heat extraction, Appl. Energy 78 (2) (2004) 159–177.